Supporting information for

Meta-stable structures in cluster catalysis from first-principles: Structural ensemble in reaction conditions and meta-stability triggered reactivity.

Geng Sun[&], Philippe Sautet[&,ç,*]

[&]Department of Chemical and Biomolecular Engineering, University of California, Los Angeles, Los Angeles, California 90095, United States

[ç]Department of Chemistry and Biochemistry, University of California, Los Angeles, Los Angeles, California 90095, United States

Table of Contents

1   Details on density functional theory calculations

All the structures in MGA explorations have been re-calculated by density functional theory (DFT) after the optimization by the high dimensional neural network potential (HDNNP). These DFT calculations are carried out with the VASP package[1-3], in which clusters are put in a box, whose size ensures that the minimum distance between the cluster and all periodic images is at least 11.0 Å. The energy cutoff for plane waves is 250 eV. Since we are studying clusters, gamma point only k-mesh is used throughout this work. The PBE functional is used for describing the electronic exchange-correlation energy[4] during MGA optimizations. Throughout this work, structure optimizations are used to reduce the maximum force residues to a value smaller than 0.01 eV/Å for the optimized structures. Only Pt_{13} clusters are optimized with spin-polarized calculations during GA calculations, in which the magnetization is optimized automatically. The vibrations of low energy structures (including all low energy meta-stable ensemble (LEME)) are analyzed to verify that the structures are true minima.

After the GA exploration, all the LEME structures are refined by optPBE-vdW functional[5] since it shows a better accuracy for Pt cohesive energy and H absorption energy on Pt[6]. In this refining step, all the calculations are spin-polarized with 400 eV energy cutoff for plane waves, and the results show that all the $Pt_{13}H_{18}$ and $Pt_{13}H_{26}$ clusters have no magnetization density. The magnetization of bare Pt_{13} clusters is optimized automatically in SCF calculation. The automatic scheme may be not adequate for obtaining the electronic ground state, while, the detailed study of magnetic moment of Pt_{13} clusters requires explicitly description of spin-orbit coupling[7-9], which is beyond the scope of current work. Therefore, we only exploits the automatic spin-polarized optimizations throughout this work.

In the application part, the H adsorption energies on $Pt_{13}H_{26}$ clusters are calculated with optPBE-vdw functional with a energy cutoff of 400 eV. The energies in methane activation are calculated by PBE functional and PBE-dDsC[10] with an energy cutoff of 400 eV. Transition state structures are firstly optimized by the Dimer method implemented in the VTST code and VASP. Then transition states are verified by vibrational analysis and IRC calculations.

The genetic algorithm, vibration analysis and thermodynamics analysis (including the free energy calculation from ideal gas limit or Harmonic Oscillator Approximation) are conducted with ASE package[11].

2 Details of vibrational analysis and free energy calculations.

The vibrational analysis and free energy calculation are conducted by the ASE code[11]. The finite difference method with $\delta = 0.015$ Å is used to evaluate the vibration frequencies. This method displaces every atom in x+, x-, y+, y-, z+, z- directions respectively to get a mass-weighted Hessian matrix F. Diagonalization of F will produce a series of eigenvalues λ_i. At the end, the frequencies will be $\nu_i = \sqrt{\lambda}/2\pi$.

The ideal-gas approximation and harmonic approximation implemented in ASE thermodynamics module[11] is used for evaluating the free energies for H_2 and $Pt_{13}H_x$ clusters respectively.

The ideal-gas approximation is used for evaluating the free energy of H_2 gas, where the free energy is calculated by:

$$G(T,P) = H(T) - TS(T,P) \tag{S1}$$

The enthalpy $H(T)$ is a function of temperature:

$$H(T) = E_{elec} + ZPE + \frac{7}{2}k_BT + \sum_{i=1}^{N_{DOF}} \frac{h\nu_i}{e^{\frac{h\nu_i}{k_BT}} - 1} \tag{S2}$$

$S(T,P)$ is calculated by:

$$S(T,P) = S(T,P^\theta) - k_B\ln\frac{P}{P^\theta} = S_{trans} + S_{rot} + S_{vib} - k_B\ln\frac{P}{P^\theta} \tag{S3}$$

Where,

$$S_{trans} = k_B\left\{\ln\left[\left(\frac{2\pi Mk_BT}{h^2}\right)^{\frac{3}{2}}\frac{k_BT}{P^\theta}\right] + \frac{5}{2}\right\} \tag{S4}$$

Where k_B is Boltzmann constant, h is Planck constant, M is the mass of the gas molecule, T is the temperature. The rotational entropy S_{rot} is calculated as:

$$S_{rot} = k_B \left[\ln \left(\frac{8\pi^2 I k_B T}{\delta h^2} \right) + 1 \right] \qquad S5$$

Where I is the momenta of inertia, and δ is symmetry number ($\delta = 2$ for H₂ gas). The vibrational entropy S_{vib} is expressed as:

$$S_{vib} = k_B \sum_{i=1}^{N_{DOF}} \left[\frac{h\nu_i}{k_B T \left(e^{\frac{h\nu_i}{k_B T}} - 1 \right)} - \ln \left(1 - e^{-\frac{h\nu_i}{k_B T}} \right) \right] \qquad S6$$

where, N_{DOF} is number of freedom for H₂ gas (which equals to one for H₂ gas).

For Pt₁₃Hₓ clusters, harmonic approximation is used to evaluate the free energies. Therefore, only the vibrational contributions are considered.

For the enthalpy:

$$H(T) = E_{elec} + ZPE + \sum_{i=1}^{N_{DOF}} \frac{h\nu_i}{e^{\frac{h\nu_i}{k_B T}} - 1} \qquad S7$$

And for the entropy:

$$S = k_B \sum_{i=1}^{N_{DOF}} \left[\frac{h\nu_i}{k_B T \left(e^{\frac{h\nu_i}{k_B T}} - 1 \right)} - \ln \left(1 - e^{-\frac{h\nu_i}{k_B T}} \right) \right] \qquad S8$$

At the end, the free energy is calculated as:

$$G(T) = F(T) = H(T) - TS(T) \qquad S9$$

3   Procedures to train the HDNNP potential.

Training a neural network potential currently relies a lot on the users' experience. The quality of final NN must be verified by numerical experiments, so there is no prior-knowledge of the quality of an NN potential. Meanwhile, there are practical tips that are helpful to train a good HDNNP potential discussed in recent papers[12-13]. In this work, we followed the basic routines mentioned in

previous publications. The first step to train a NN potential is to construct a database that is sufficiently representative. Since NN is easy to interpolate but difficult to extrapolate, the accurate prediction is only acquired when the unknown structure is located in the interpolation region in the training database[12, 14]. Hence, the selection of the training database is very important. After the construction of the database, the training can be conducted with routine error residence minimization algorithm. One of the important tunable parameters for a NN potential is its architecture. A typical architecture is notated as X-N-N-1, where X is the dimension of input parameters, which is determined by the symmetry function set, and N is the number of nodes in each hidden layers. If three hidden layers are used, the architecture is labeled as X-N-N-N-1. Usually, several different architectures are used for training NN against the same database. Finally, only the NN potential that balances architecture (model complexity) and accuracy should be used for productive calculations. If the architecture is too small, NN potential cannot flexibly capture the complex interactions, but if the NN has a too large architecture, the NN is easily over-trained and computationally expensive.

In this work, we aim at studying the Pt_nH_x clusters with genetic algorithm (GA), during which many structure optimizations from high energy configurations will be conducted. Hence, it is vital to include the high-energy configuration structures in the training database; otherwise, the structure optimization would be misleading. We first set up a group of initial structures with various compositions: The formula of the cluster is noted as Pt_nH_x, where n runs from 6 to 20 and the corresponding x runs over from 0 to 3n. All the reference structures are isolated clusters. Then we used an iterative approach to simultaneously train the neural network and build up the database. The scheme of this training procedures is illustrated in Figure S1. The strategy used here is similar to the work of Artrith[13] in NN training and other ML training procedures.[15] The iterative training including 5 steps:

a) Monte Carlo simulations with NN(i)
b) Selection of NN samples (energy is calculated by NN(i))
c) Evaluation of DFT sample (energy is calculated by DFT)
d) Convergence check
e) Training a new potential NN(i+1) if step (d) is not converged.

The details are described in the following. The main idea here is to take advantage of efficient NN to quickly sampling configuration space and generate new structures that are then re-calculated by

DFT and added into the reference pool. With the increasing number of structures in the reference pool, the accuracy of newly trained NN potential is supposed to improve.
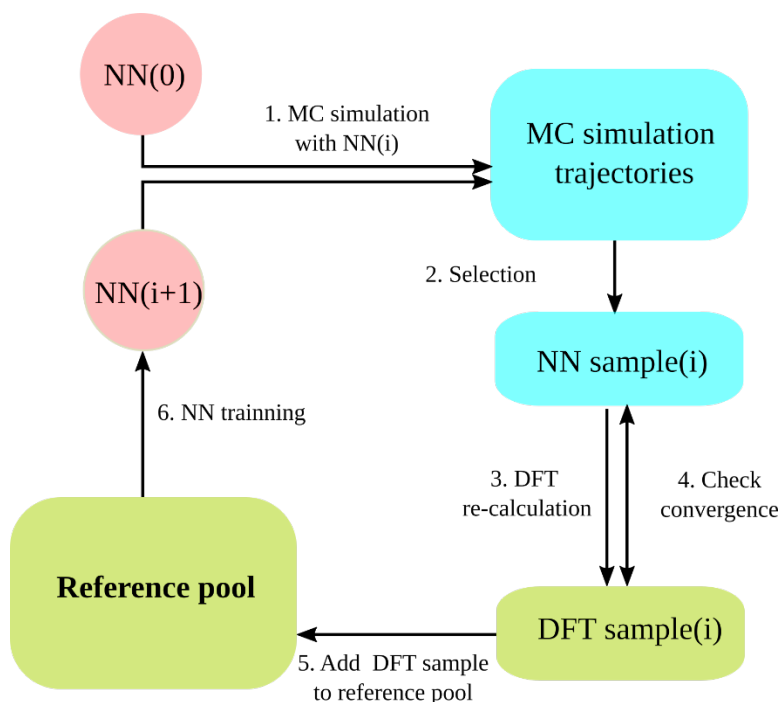

Figure S1. An iterative strategy for training NN as well as generating the reference database

The details for the training of the NN potential is described here:

Monte Carlo simulations with NN: With a pre-trained NN(i) (NN(i) means NN potential in the ith iteration (NN(0) is trained from a very small database). Standard Metropolis Monto-Carlo (MC) simulations are launched with random initial structures (compositions are selected from one of Pt_nH_x set). Normally 200 MC simulations are carried out simultaneously. The temperature of every MC simulation is also randomly assigned within 400~2000 K. The MC simulation is aimed at quickly sampling the configuration space with computationally efficient HDNNP. High temperatures are included in order to incorporate high energy structures in the database.

Selection of NN samples: All MC simulations run 10000 steps. The first 5000 steps are neglected to remove unreasonable structures. Then the structures are selected every 50 steps during the last 5000 MC steps in order to reduce the similarity of the selected structures. Some of those selected structures have too close inter-atomic distances or are fractured, therefore they are abandoned. In the end, if the total number of sample collection (from all MC simulations) is larger than 10000,

then only 5000 of them are selected. This step will produce about 2000~8000 structures. They are called the NN sample.

Evaluation of DFT sample: All the NN sample structures from the previous step are re-calculated by DFT. In this work, the DFT calculations are carried out using the VASP package[2-3, 16] with Perdew–Burke–Ernzerhof (PBE) exchange-correlation functional[4]. All the calculations are single point calculations without structure optimizations. Clusters are separated with their images by at least 11.0 Å in all the directions. Energy cutoff for the plane waves is 250 eV and only non-spin polarized calculations are considered in this step.

Convergence check: After step 3, the energy difference between NN sample (evaluated by NN(i)) and DFT sample (evaluated by DFT) is calculated. The error is measured by the value of root-mean-square error (RMSE), which is defined as Equation S(10):

$$\text{RMSE} = \sqrt{\frac{\sum_{j=1}^{M}\left[\frac{\left(E_j^{NN(i)} - E_j^{DFT}\right)}{N_j}\right]^2}{M}} \qquad S10$$

Where M is the size of NN sample (and DFT sample), N_j is the number of atoms in structure j. Hence, the calculated RMSE is the per-atom error. Because the initial NN(0) is trained against only a small database, NN(0) is expected to show a large error in this step. With the size of the reference database getting larger and larger, the quality of acquired NN is supposed to get constantly improved. In the meanwhile, the acquired NN potential is more and more robust.

Training a new NN potential: All the "good" structures in the DFT samples (max force is below 10.0 eV/Å) with their DFT energies and forces are merged into the reference pool. The reference pool is a collection of all the previous DFT calculations. Then the new reference pool is used for training the next generation NN. The ænet (atomic energy network) package developed by Artrith et al.[13] is used through this work for training and predicting energies. The parameters of symmetry functions are listed in Table S1. We also tested other symmetry function parameters, but no significant improvements were observed for the database in this work.

Table S1 Symmetry function parameters. In this work, we are using the same parameters for both H and Pt element. The meaning of different parameters are shown in Equation (1)-(3) in the main text

η_1(Bohr^{-2})	0.001, 0.01, 0.02, 0.035, 0.06, 0.1, 0.2, 0.4
η_2(Bohr^{-2})	0.0001, 0.003, 0.008, 0.025
ζ	1.0, 2.0, 4.0
λ	1.0, -1.0
R_c(Å)	6.5

Table S2 shows the results of the iterative training. In order to train the NN, the reference database is always randomly split into two parts. One part (about 80-90 % of reference pool) is used for training the NN, the rest of the structures are used for monitoring the quality of the NN (designated as control set in the following). The best NN is selected by an early-stop strategy, which is demonstrated in the sketch of Figure S2. The NN training with different architectures are shown in Table S3 and finally, we choose X-5-5-1 for following productive calculations (X=88 in this work). NN with larger architectures do not significantly improve the accuracy, instead they are more computationally expensive because of larger parameter sets.

Table S2 The convergence check results for iterative NN training. The architecture of the neural network used here is X-5-5-1. In this step, we calculated two type of errors. The first one includes all the structures (4th column of Table S2), whereas the second one dismisses those structures whose maximum DFT-calculated force (DFT result) is larger than 10 eV/Å(3rd column). At the early stage, due to the poor quality of NN, many structures in the NN samples have large force components indicating that NN potential does not lead the MC simulations into reasonable configurations regions. So we did not include those structures in further NN training. If we neglect those bad structures in convergence check, the errors are listed in the third column, otherwise, the results are listed in the fourth column. The iterative training results show that in the last step MC simulations, all NN simple structures are also reasonable structures in DFT calculations, which indicates that the simulations with this NN potential will be more stable.

Iteration	Training set Error/control set Error(meV/per-atom)	Convergence check error(meV/per-atom)[a]	Convergence check error(meV/per-atom)[b]
0		270	
1	16/25	302	
2	19/20	79	
3	22/24	65	1005
4	17/20	49	
5	23/24	42	
6	20/21	28	73
7	21/22	39	39
8	23/23		

[a] The convergence check doesn't include the structures with $f_{max} > 10$ eV/Å or E(per-atom) > -3.0 eV.

[b] The convergence check includes all the structures.

Table S3 Errors of HDNNP with different architectures. Values shown in this table are RMSE of per-atom (meV/atom).

#layer	2 hidden layers		3 hidden layers	
#nodes	training set	Control set	Training set	Control set
5	23	23	23	23
10	20	21	19	20
15	18	19	19	21
20	18	19	20	21
25	19	20	19	20
30	17	19		
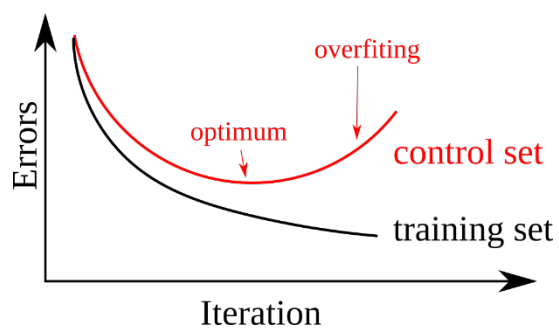
Figure S2 The early stop scheme in HDNNP training. At the beginning, the errors of the training and control set decrease simultaneously, but after several steps, the error of control set may begin increasing. The increasing of errors for control set indicates the over-training of the NN.

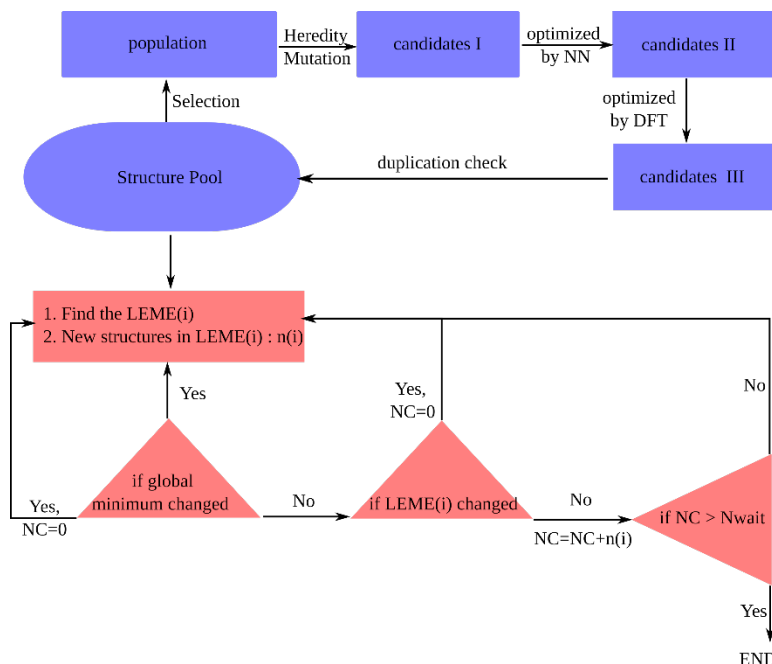# 4 Details of Modified Genetic Algorithm(MGA)

4.1 Flowchart of MGA

Figure S3 The flowchart of MGA. The purple boxes (upper) show the routines for genetic algorithm. The red boxes show the procedures to check the convergence of MGA

The flowchart of MGA contains two main parts and is shown in Figure S3. The first part (upper region with purple boxes) is the genetic algorithm. First, a generation is selected from the database pool. The sizes for a generation in MGA optimizations are 80, 100 and 120 respectively for Pt_{13}, $P_{13}H_{18}$ and $Pt_{13}H_{26}$. $E_{window} = 0.5$ eV is used for defining the LEME and that is sufficient to cover all the thermodynamically accessible metastable isomers. The stopping criterion of MGA, i.e. N_{wait} is set at 100 for the Pt_nH_x clusters. Then the normal heredity and mutation operations are carried out to produce candidate structures (candidates(I)). Normally the structures of candidates (I) are far from the local minima, so HDNNP is first exploited for structure optimizations and produces candidates (II). Then, DFT calculations are used to refine the structures of candidates(II). Before the DFT refining, the structures in candidates(II) are filtered by their geometries. If the structures are fractured, they would be dismissed without further refining. In this study, all the reasonable structures are refined by DFT calculations. However, in principle, one can safely dismiss some high energy structures in candidates(II) (with NN potential predicted energy) to further reduce the computational cost. A buffer energy window (with taking the error of HDNNP

potential into account) can be used to select this energy range. Since some structures in candidates(III) are the same as those in the structure pool, duplication check[17] is used to keep all the pool structures unique.

4.2 Convergence of MGA calculations

The *structure pool* database (in Figure S3) is inspected simultaneously with GA optimizations. First, the low energy meta-stable ensemble (LEME) is selected from the *structure pool*. The LEME is defined as the structures in the structure pool database, whose energy lies between the current putative global minimum energy E_m and $E_m + E_{window}$. The LEME structures at iteration i is notated as LEME(i). Then the number of new structures that appears in the database since last inspection is also counted, the size of accretion, is noted n(i). $n(i)$ counts the new structures in structure pool no matter whether they are LEME structures. If the putative global minimum has changed since last inspection, the variable NC is set as 0, otherwise we check whether LEME(i) is identical with previous LEME(i − 1). If LEME(i) is identical to previous LEME(i − 1), we would add n(i) to NC. NC indicates that we have not found any new LEME structures in NC consecutively successful kicking operations (a successful kicking is defined as a kicking that leads to new structure). Finally, if NC is already larger than a prior chosen parameter N_{wait}, the MGA exploration is considered as converged.

4.3 Validation of modified genetic algorithm by LJ$_{38}$ clusters.

In order to validate whether the proposed MGA can reliably find the ensemble of low-energy structures, we explored a prototype system: the 38 atoms Lennard-Jones cluster (LJ$_{38}$). LJ$_{38}$ consists of 38 single-element atoms interacting with a Lennard-Jones potential. the total energy of LJ$_{38}$ cluster is expressed as:

$$E = 4\varepsilon \sum_{i<j} \left\{ \left(\frac{\sigma}{r_{ij}}\right)^{12} - \left(\frac{\sigma}{r_{ij}}\right)^{6} \right\} \qquad S11$$

LJ$_{38}$ has a double-funnel energy landscape[18], which is challenging for global optimization methods and acts as an example for validating global optimization methods[19-20]. The first three stable structures of the LJ$_{38}$ cluster are reported by Wales et al.[18]. The most stable structure is an fcc

truncated octahedron with energy $E_1 = -173.9284\varepsilon$. The energies of second and third most stable structure energie are $E_2 = -173.2524\varepsilon$ and $E_3 = -173.1343\varepsilon$ respectively.

We first compared the efficiency of MGA and random searching method. The atoms are randomly generated in a box and this routine is essentially the same as the routine for generating initial structures in the GA algorithm. Then the cluster is optimized until the max residue force is below $1 \times 10^{-6}\varepsilon/\sigma$, where we are using $\sigma = \varepsilon = 1.0$ for both random searching and MGA. After the optimization, only the compact structures are collected for subsequent analysis and the fractured structures are dismissed if two groups are separated by larger than $1.8 \times \sqrt[6]{2}\sigma$, where $\sqrt[6]{2}\sigma$ is the equilibrium bond length between two Lennard Jones atoms. The size of generation is 200 in the MGA, where every structure is unique and the duplicated structures are removed according the same scheme as in the work of Hammer et al.[17] In every interval between two epochs during GA, all the structures between the currently putative global minimum energy E_m and $E_m + E_{window}$ are selected and they are compared with previous selections. Here for LJ$_{38}$ clusters, $E_{window} = 2.5\varepsilon$ is used in this work. It should be noted that for the LJ$_{38}$ cluster, the E_{window} is chosen arbitrarily without any physical bases. The only concern is that the number of structures located in the LEME should be reasonable. If the energy window is too large, there will be too many structures because the density of states is every large for high energy configurations, therefore, the convergence criterion will be never achieved. For the LJ$_{38}$ cluster, we used the disconnectivity graph described in Wales paper[18] as a reference to determine a reasonable $E_{window} = 2.5\epsilon$, which contains several tens of structures and also covers structures in two funnels. Therefore, we think this parameter is able to demonstrate the efficiency of the proposed MGA. Fortunately, for the cases of many practical catalyst models, a small window like $E_{window} = 0.5$ eV is a reasonable criterion to get all the thermodynamically accessible isomers and there are only a limited number of structures located in this range. We are using the $N_{wait} = 450$ in the LJ$_{38}$ cluster example. Of course, the larger the N_{wait} is, the more accurate the final results will be, but the exploration will be more expensive.

The results of this example are illustrated in Figure S4. The total number of structure optimizations used is also given. Figure S4 shows that the random searching method uses 10 times more structure optimizations than the MGA. Obviously, the MGA launched structures optimizations which focused on the low energy configuration space, while the random searching method results in many

optimized structures which are higher in energy and not attractive. The result demonstrates the key feature of GA: it tends to focus on the low energy configuration space to reduce the total computational cost. The Figure S4(b) shows the LEME found in MGA and compared with those found in random searching. It is clearly shown that even though the structures found in MGA are not exactly the same between several tests, these MGA runs found the all the important low energy structures and also show the correct features of potential energy surface (DOS). Meanwhile random searching method missed many LEME structures even though it used 10 times more structures optimizations. This validation calculation gives us confidence that MGA could reliably uncover the low energy structures with high efficiency.
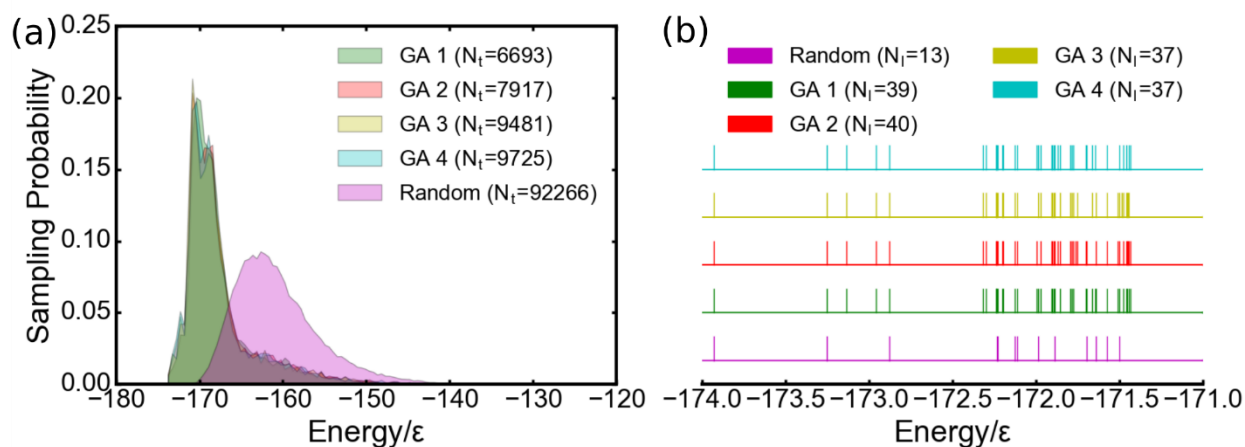
Figure S4 The validation of MGA using LJ$_{38}$ cluster. (a) illustrates the normalized energy distribution of the optimized structures from MGA (notated with GA) and random searching methods. MGA is launched several times for comparison. (b) shows all LEME structures ($E_{window} = 2.5\epsilon$) found by MGA or random searching method.

5 Applications: LEME of $Pt_{13}H_x$ clusters in HER and methane activation catalysis.

5.1 Numbers of structures in the LEME explorations.

Table S4 numbers of structures in the LEME and structure pool.

Cluster	Pt_{13}	$Pt_{13}H_{18}$	$Pt_{13}H_{26}$
Size of structure pool	2644	1589	1966
Size of LEME	49	20	19

5.2 Structures of LEME
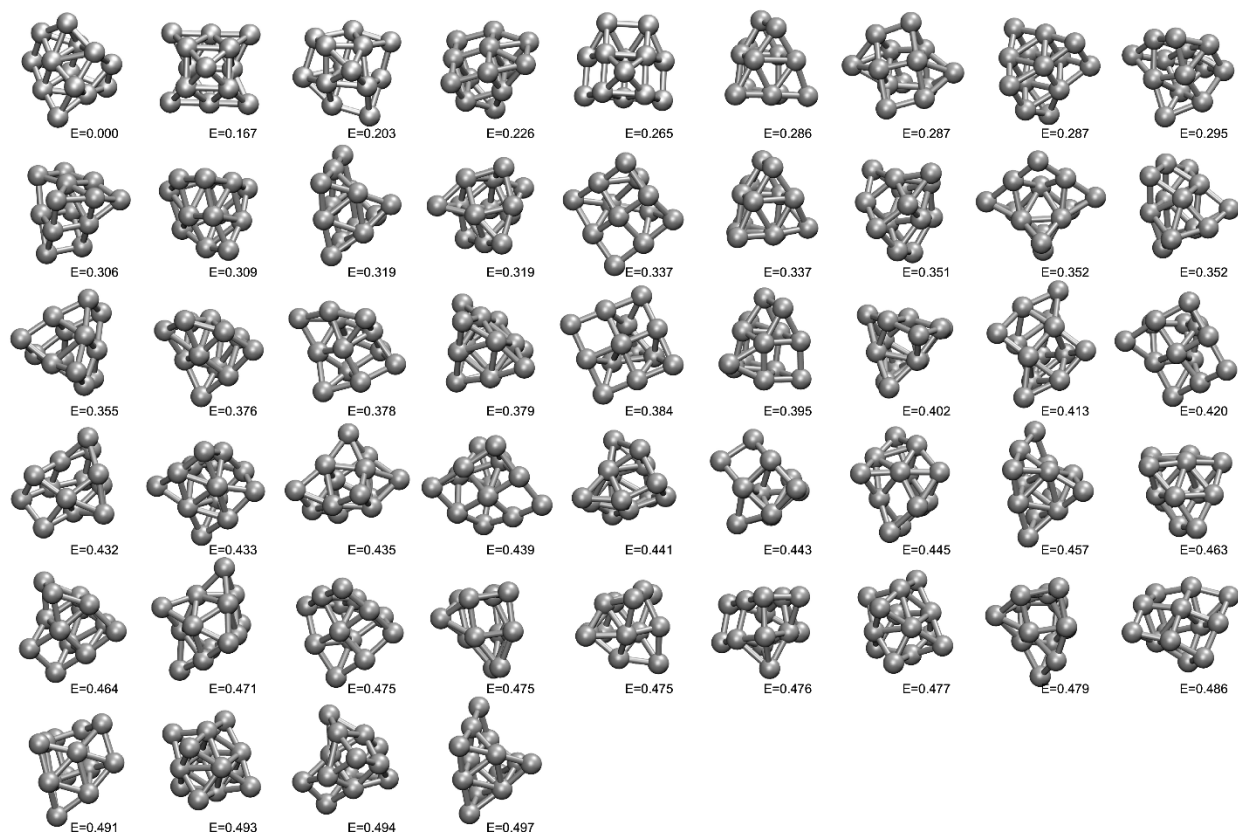
Figure S5 LEME structures of bare Pt_{13} clusters and their relative energies with respect to the global minimum (eV) . There are in total 49 unique structures in an interval of 0.5 eV. All energies are calculated with the optPBE-vdW functional.

E=0.000 E=0.006 E=0.194 E=0.248 E=0.280

E=0.280 E=0.296 E=0.302 E=0.382 E=0.396

E=0.411 E=0.418 E=0.423 E=0.425 E=0.438

E=0.464 E=0.475 E=0.475 E=0.475 E=0.480
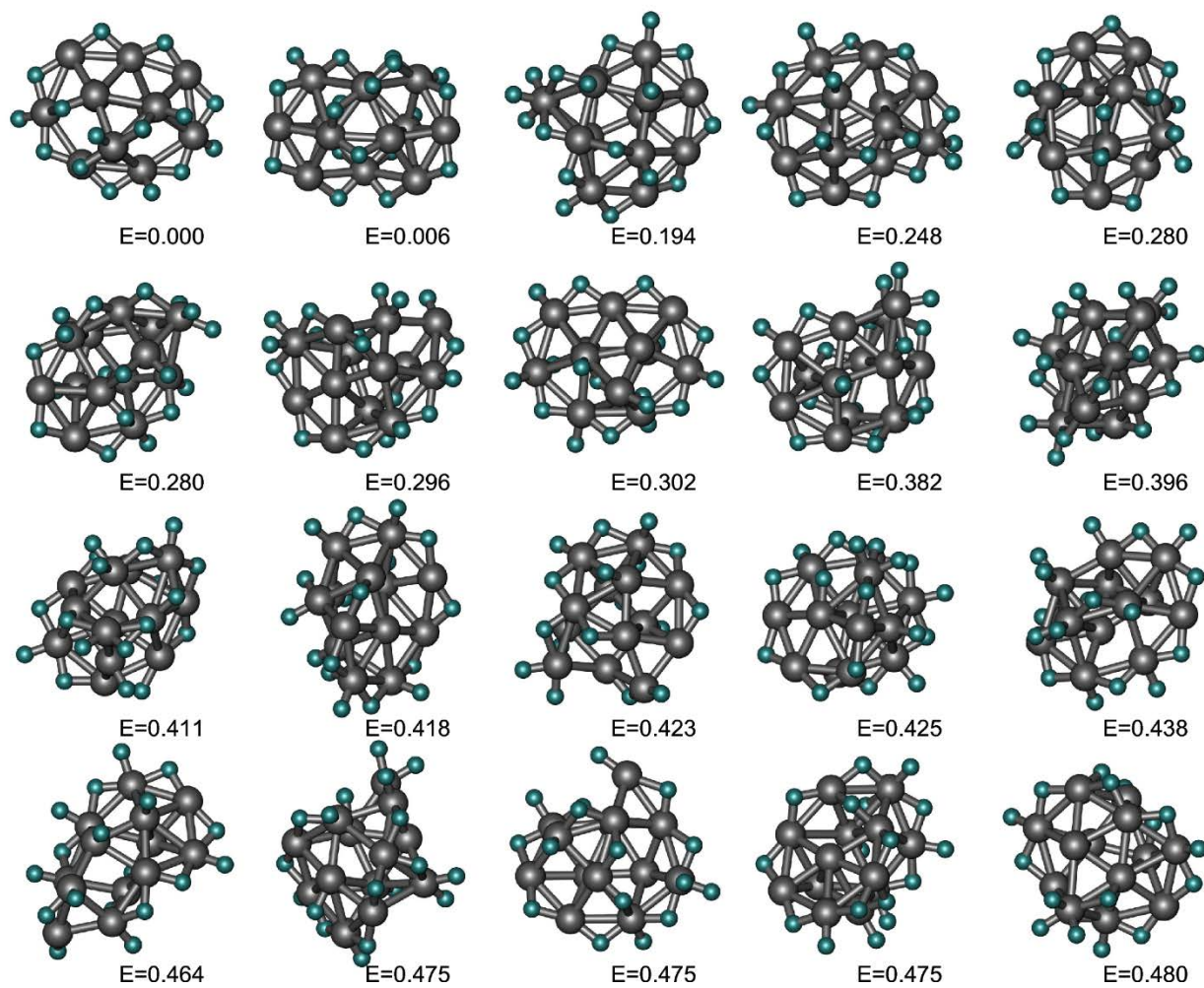
Figure S6 . The LEME structures of $Pt_{13}H_{18}$ and their relative energies with respect to the global minimum (eV). There are 20 structures in the LEME. All energies are calculated with the optPBE-vdW functional.
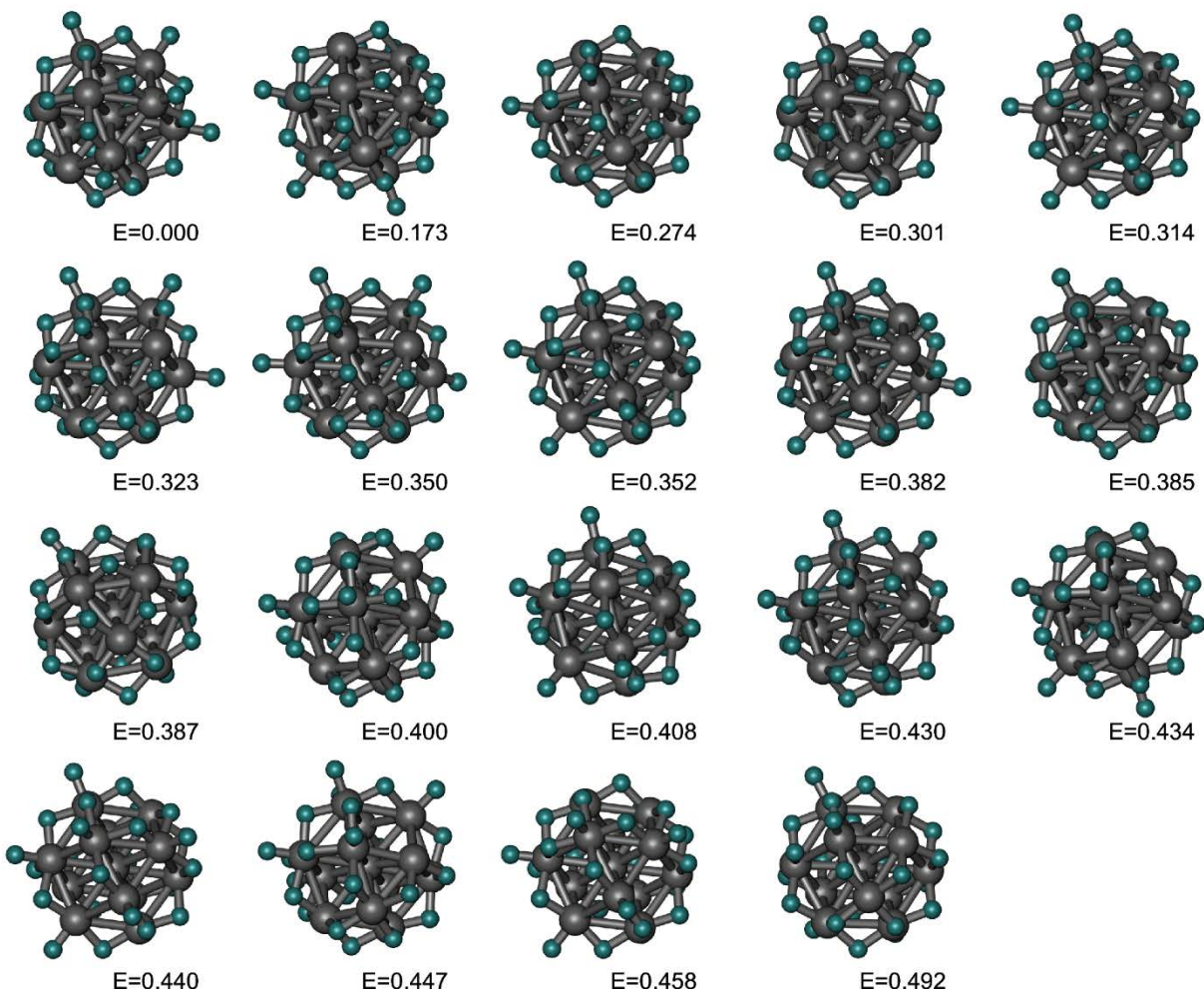
E=0.000　　E=0.173　　E=0.274　　E=0.301　　E=0.314

E=0.323　　E=0.350　　E=0.352　　E=0.382　　E=0.385

E=0.387　　E=0.400　　E=0.408　　E=0.430　　E=0.434

E=0.440　　E=0.447　　E=0.458　　E=0.492

Figure S7 The 19 LEME structures of $Pt_{13}H_{26}$ clusters and their relative energies (eV) calculated with the optPBE-vdW functional. All the structures have a cuboctahedral Pt_{13} cores and only differ in H positions.

5.3   H adsorption sites for H covered clusters.
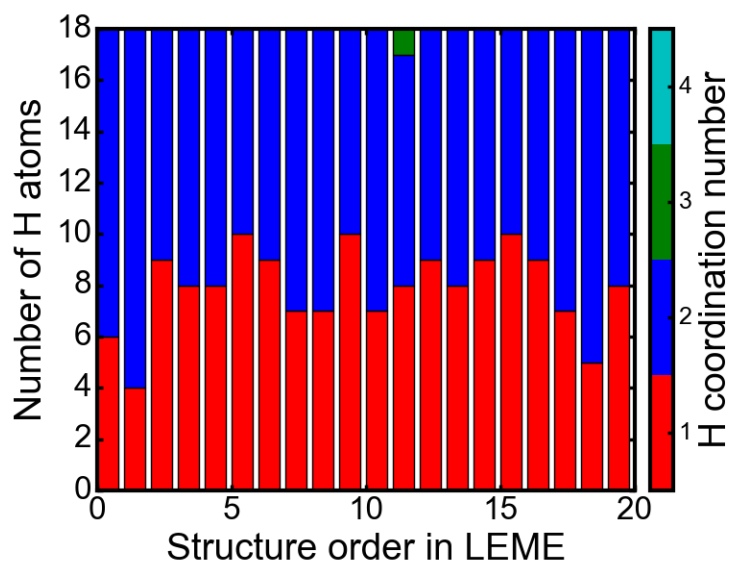
Figure S8: Distribution of coordination (1: top site, 2: bridge site, 3: three-fold hollow site) for H atoms on the 20 structures in the LEME of $Pt_{13}H_{18}$. The indexes on the x axis is the order of the stability in the LEME, where the first structure is the global minimum. The colors indicate the number of coordinated Pt atoms for the H atoms.
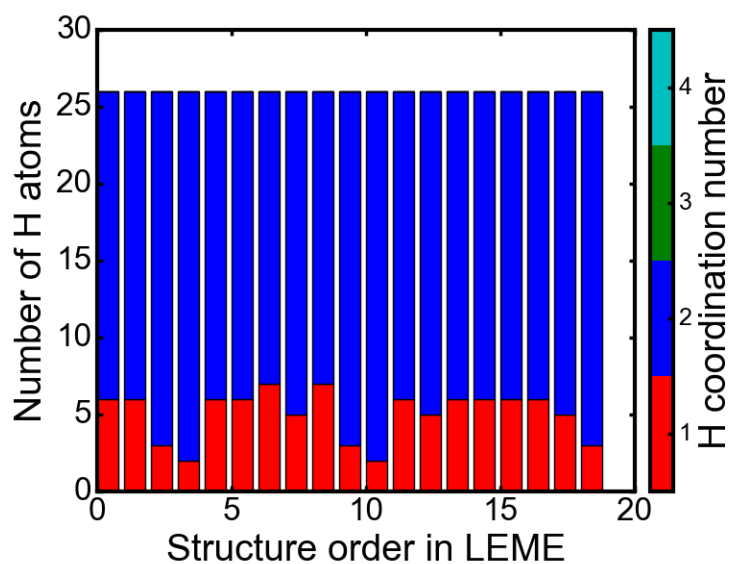
Figure S9: Distribution of coordination (1: top site, 2: bridge site, 3: three-fold hollow site) for H atoms on the 19 structures in the LEME of $Pt_{13}H_{26}$. The indexes on the x axis is the order of the stability in the LEME, where the first structure is the global minimum. The colors indicate the number of coordinated Pt atoms for the H atoms.

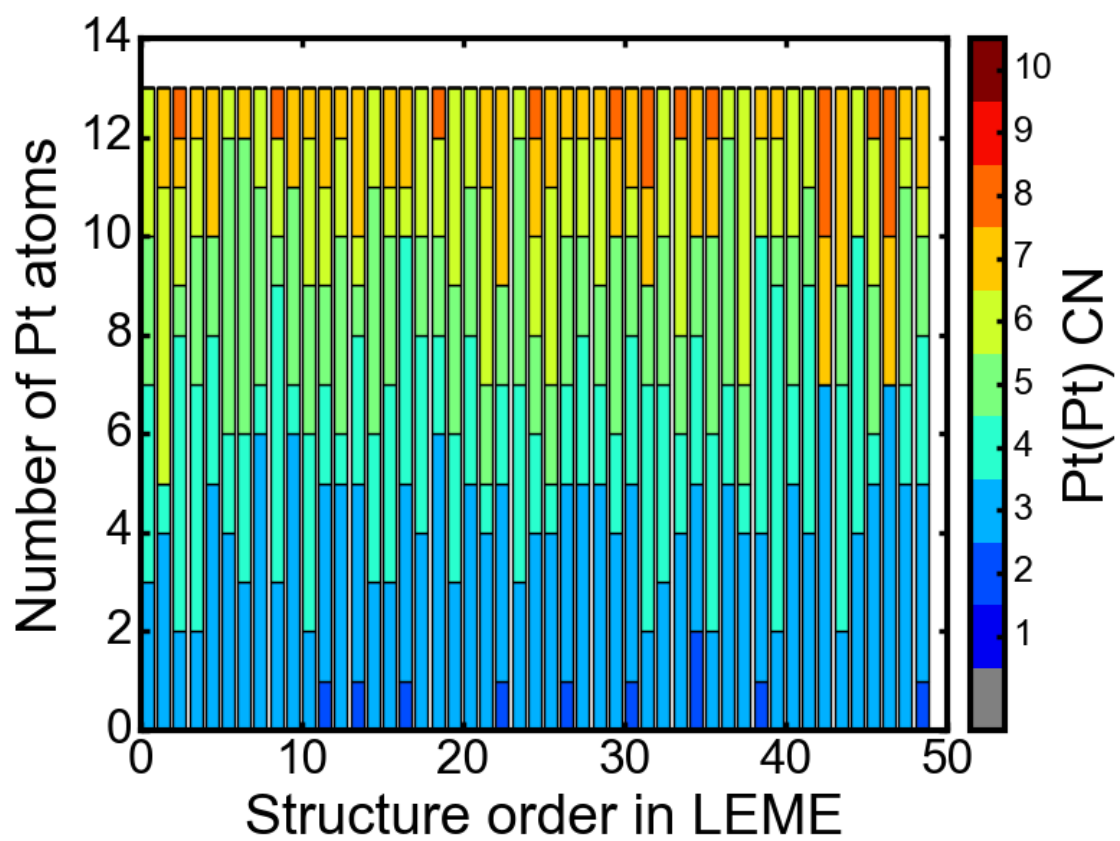## 5.4   Pt-Pt coordination analysis

Figure S10: Distribution of Pt-Pt coordination numbers (CN) for the 49 LEME structures of Pt_{13}.
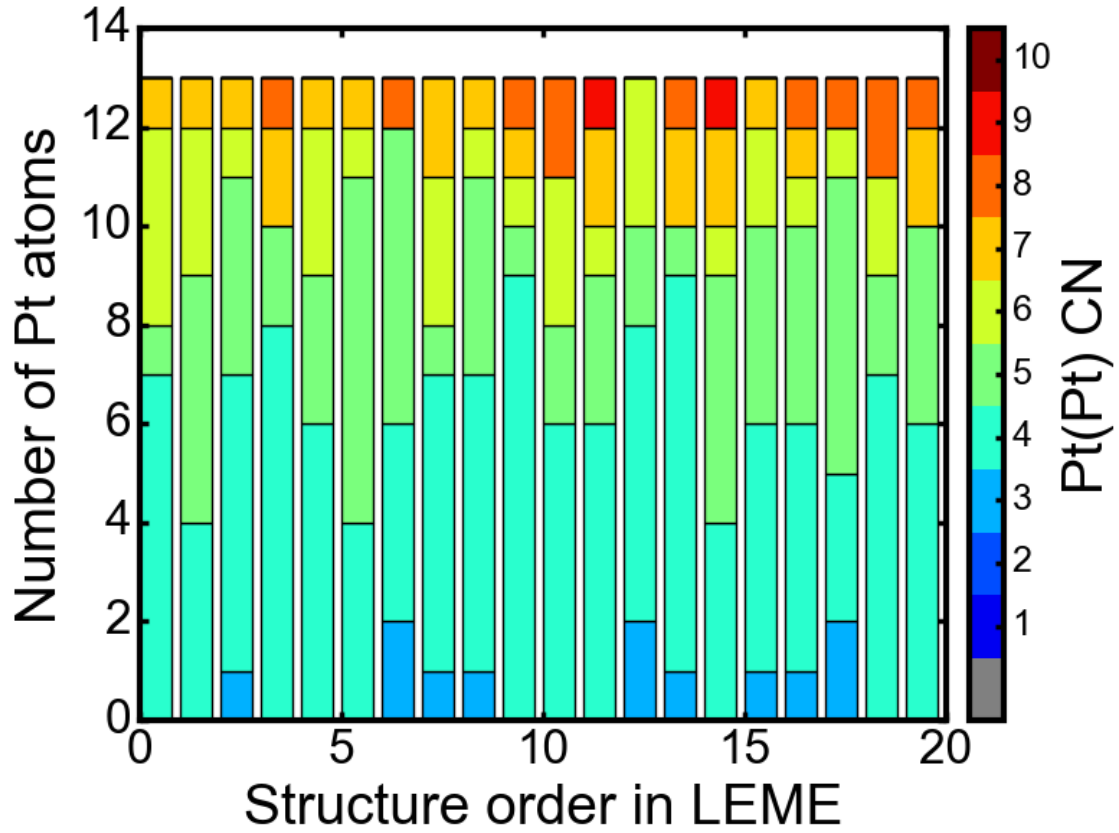
Figure S11: Distribution of Pt-Pt coordination numbers (CN) for the 20 LEME structures of $Pt_{13}H_{18}$.

5.5 Spin-orbit coupling effects on the relative stability of bare Pt_{13} clusters.

We are taking following equation for evaluation of the SOC correction to the total energy of bare Pt_{13} clusters with optPBE-vdw functional.

$$E_{optPBE-vdW}^{SOC}(i) = E_{optPBE-vdW}(i) + \left(\min\{E_{PBE}^{SOC}(i)\} - E_{PBE}(i) \right) \qquad S12$$

Where, $E_{optPBE-vdW}(i)$ is the energy of structure i in the LEME with optPBE-vdW functional. $E_{PBE}(i)$ is the energy of structure i with PBE functional without SOC. We did not optimize the structure with PBE anymore, and we only calculate its energy with PBE functional with fixing the geometry. $\min\{E_{PBE}^{SOC}(i)\}$ is the minimum energy of structure i with SOC in different quantization axis. The results show that the MAE (magnetic anisotropy energy) is small for Pt_{13} clusters. Energies of first 15 images in the LEME are corrected with SOC, which are shown in

Figure S12. It is shown that the stability order is slightly shuffled by the inclusion of SOC effects.
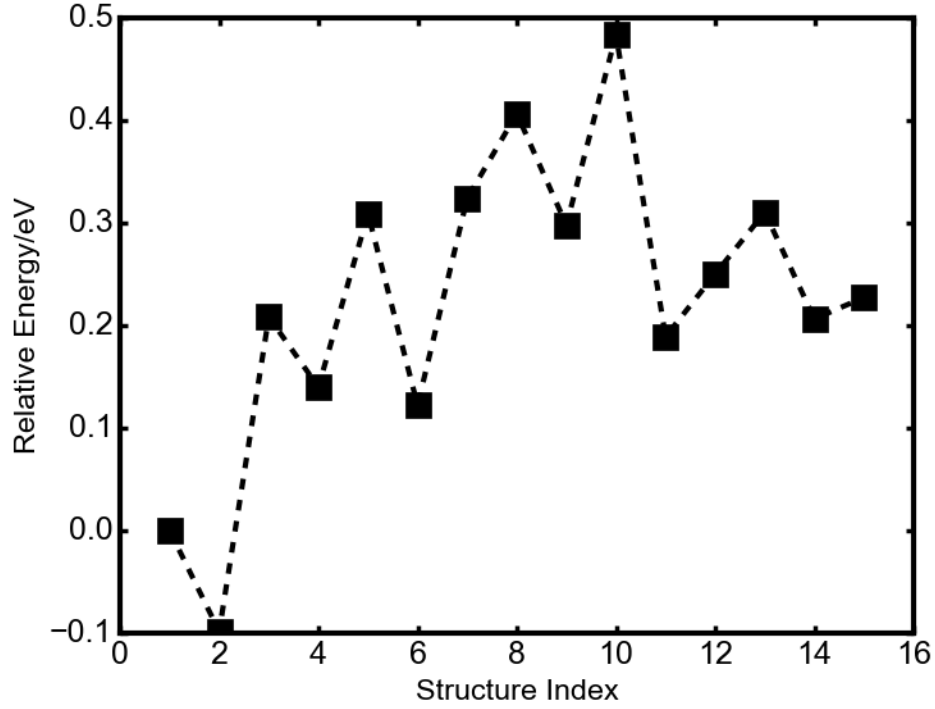

Figure S12. The stability of bare Pt$_{13}$ clusters with spin-orbit coupling (SOC).

5.6 Anisotropy of Pt$_{13}$H$_x$ clusters

The shape of the Pt$_{13}$H$_x$ clusters can be described by the anisotropy of atomic positions κ, which is derived from the gyration tensor of the atomic positions. First the gyration tensor is expressed as:

$$S_{mn} \overset{\text{def}}{=} \frac{1}{N} \sum_{i=1}^{N} r_m^i r_n^i \qquad S13$$

r_m^i is the mth Cartesian coordinate of particle i.

Once S_{mn} is diagonalized and one can get three principal moments, $\lambda_x^2 \leq \lambda_y^2 \leq \lambda_z^2$. The relative shape anisotropy is defined as:

$$\kappa = \sqrt{\frac{3}{2} \frac{\lambda_x^4 + \lambda_y^4 + \lambda_z^4}{\left(\lambda_x^2 + \lambda_y^2 + \lambda_z^2\right)^2} - \frac{1}{2}} \qquad S14$$

If the atomic positions are more spherically symmetric, κ is more close to zero, if the atomic positions are arranged in a line, the κ will be close to 1, if the atomic positions are arranged in a plane, the κ will be closed to 0.5. Therefore, according to the value of κ we can discern the cluster shapes of all the LEME structures. The results are shown in Figure S13.
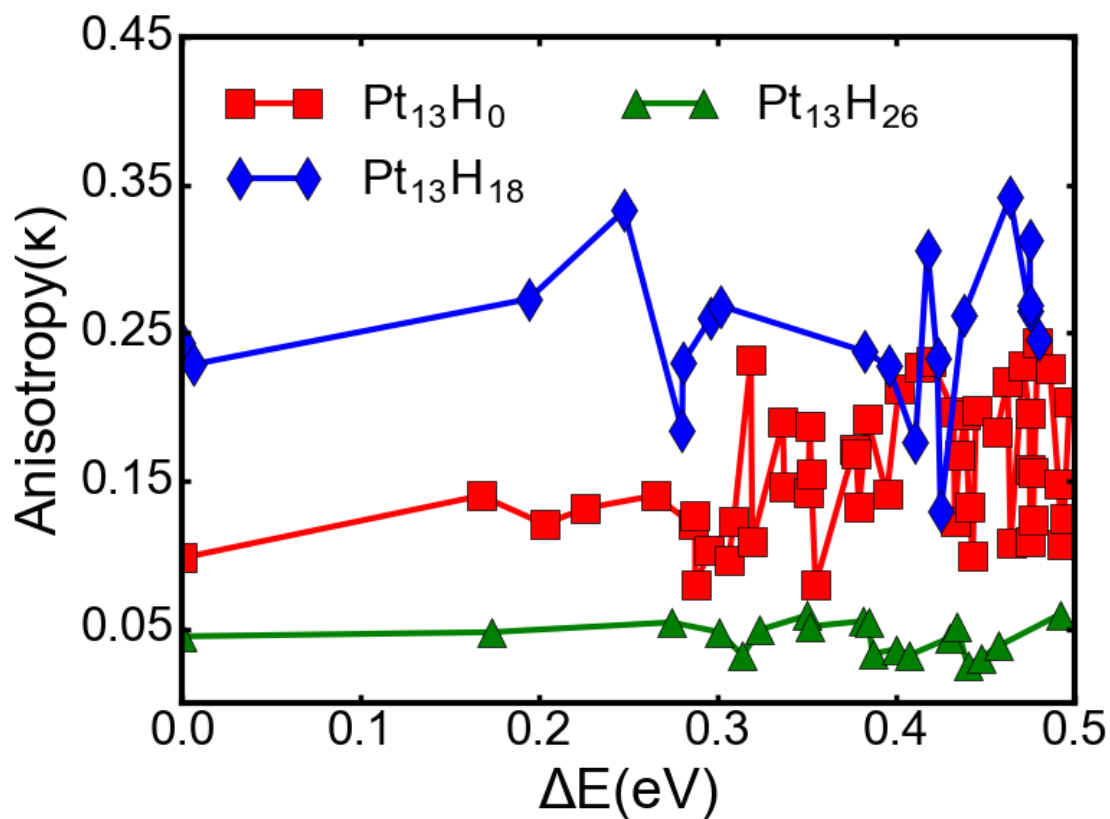

Figure S13. The anisotropy κ of the structures in the LEME of Pt_{13}, $Pt_{13}H_{18}$ and $Pt_{13}H_{26}$.

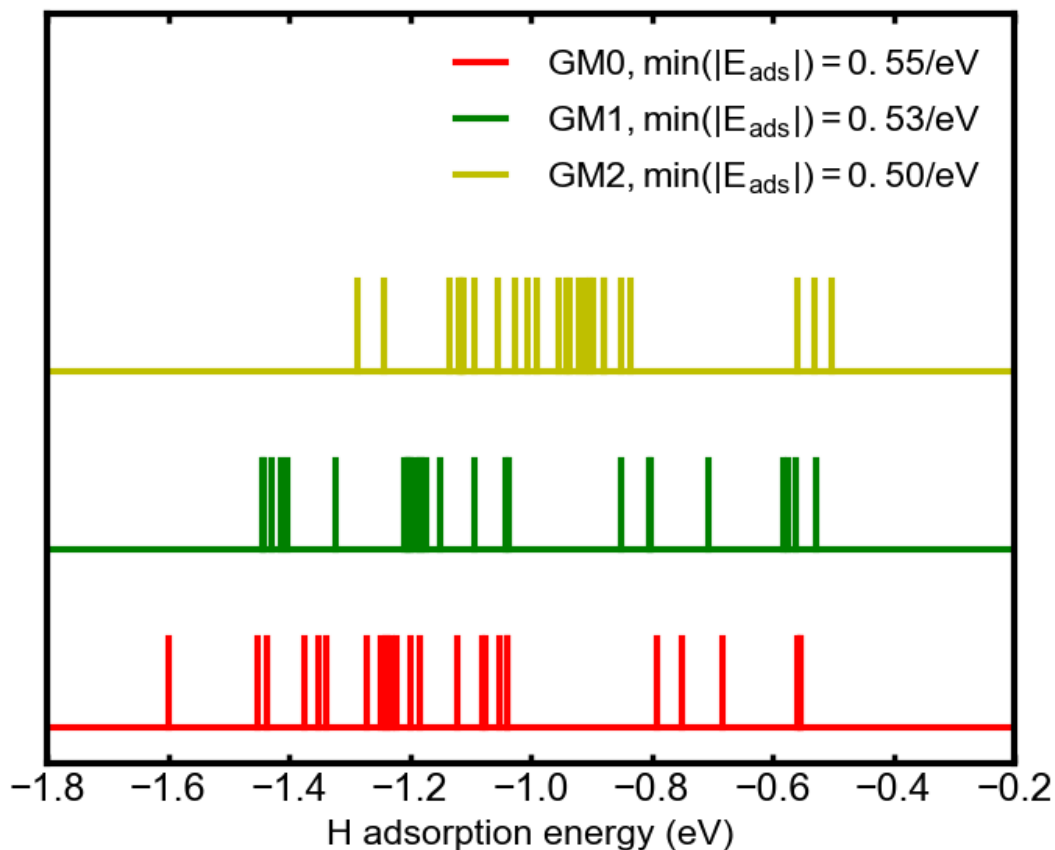## 5.7 Adsorption energies of H atoms on $Pt_{13}H_{26}$ clusters

Figure S14. Binding energies of H atoms on $Pt_{13}H_{26}$ clusters. The binding energies of each of the 26 H atoms are calculated by $E_{ads} = E(Pt_{13}H_{26}) - 0.5 \times E(H_2(gas)) - E(Pt_{13}H_{25})$, where $E(Pt_{13}H_{25})$ is calculated by removing individual H atoms and then optimizing the structure to a nearby local minimum. $E(H_2(gas))$ is the electronic energy of H_2 without entropic corrections. Only structures of GM0 (global minimum), GM1 (second most stable structure) and GM2 (third most stable structure) of $Pt_{13}H_{26}$ are considered in these calculations.
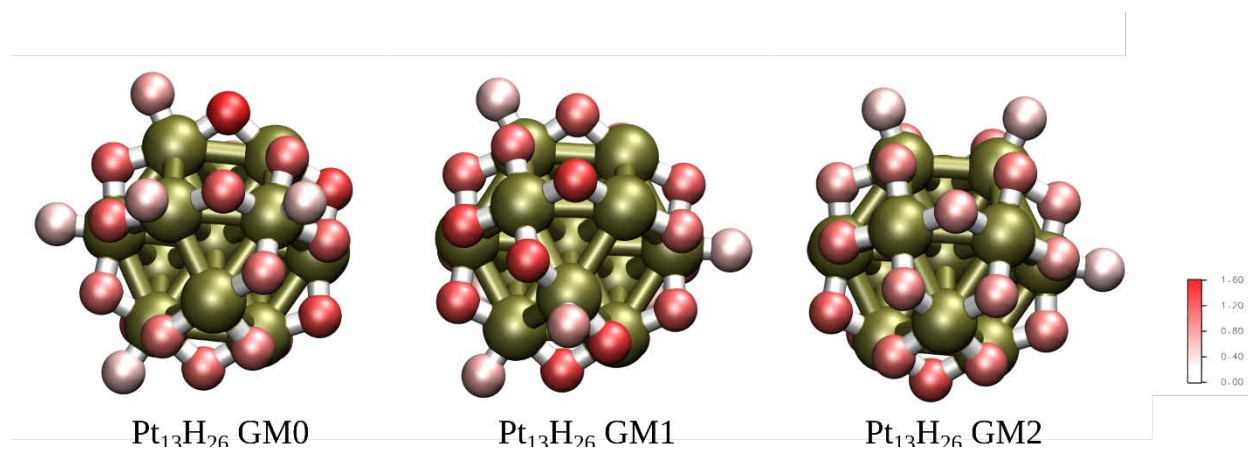
Pt$_{13}$H$_{26}$ GM0   Pt$_{13}$H$_{26}$ GM1   Pt$_{13}$H$_{26}$ GM2

Figure S15. The binding energies of H atoms on three most stable Pt$_{13}$H$_{26}$ clusters, shown as a color code (the darker is the red color, the stronger is the binding). It is obvious that the bridge site H atoms are more strongly bound than the top site H atoms.
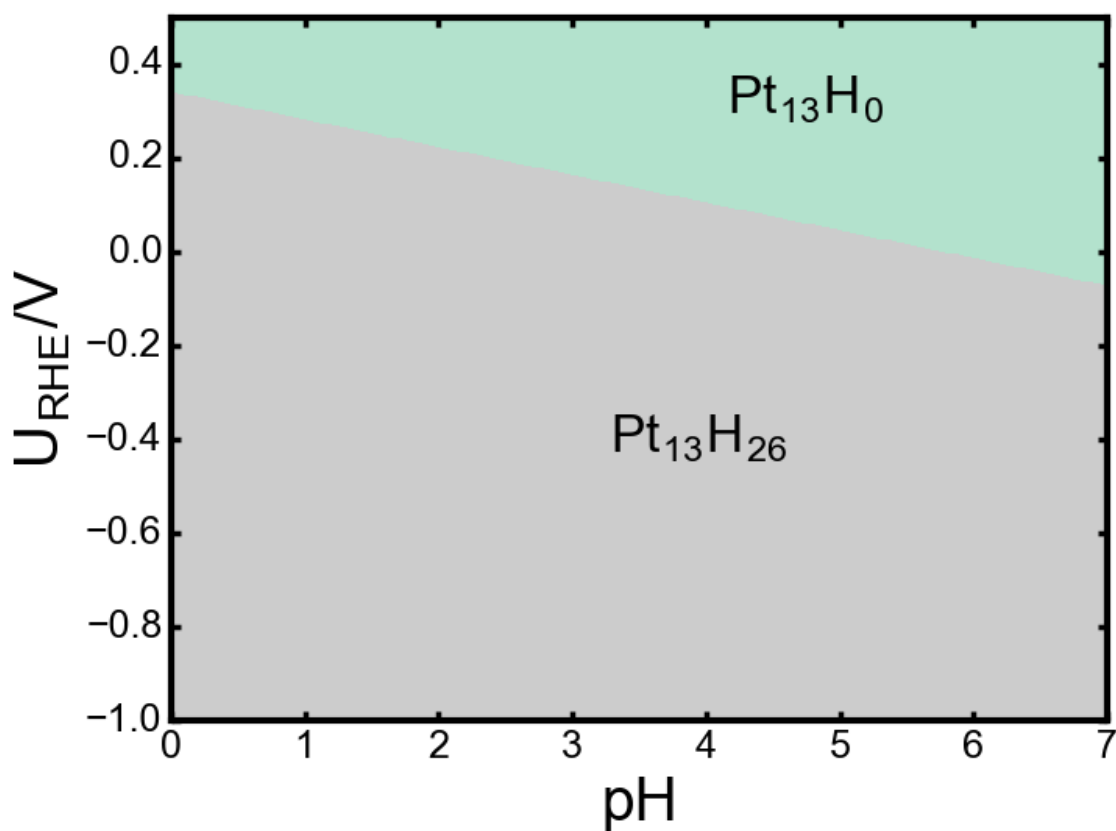
5.8 Pourbaix diagram for Pt$_{13}$-H$_x$ clusters

Figure S16 . Pourbaix diagram for Pt$_{13}$-H$_x$ cluster, comparing Pt$_{13}$H$_0$, Pt$_{13}$H$_{18}$ and Pt$_{13}$H$_{26}$. The HER reaction is often conducted in acidic conditions and at a small negative potential U_{RHE}, so that adsorption of OH on the Pt cluster is neglected. In these conditions a high H coverage (Pt$_{13}$H$_{26}$) is favored.

5.9 Calculating the contribution of Pt$_{13}$H$_{26}$ isomers for the HER reaction

The exchange current densities of different clusters are calculated by the equations obtained by Norksov and coworkers[21]:

$$i_0 = -e k_0 \frac{1}{1 + \exp\left(-\frac{\Delta G(\mathrm{H}^*)}{k_B T}\right)} \qquad\qquad S15$$

For $\Delta G(\mathrm{H}^*) < 0$ and

$$i_0 = -ek_0 \frac{1}{1 + \exp\left(-\frac{\Delta G(\text{H}^*)}{k_B T}\right)} \exp\left(-\frac{\Delta G(\text{H}^*)}{k_B T}\right) \qquad S16$$

For $\Delta G(\text{H}^*) > 0$.

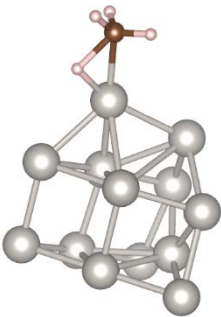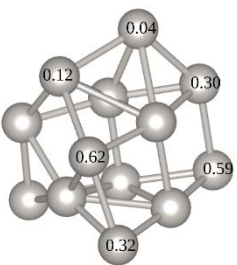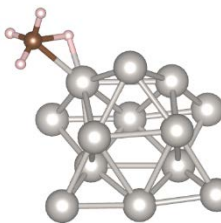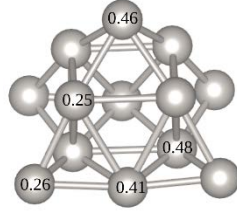$k_0 = 200 \ s^{-1} site^{-1}$ is used in above equations.

In the left part of figure 6 of main text, the dashed line is predicted with Equation S5 and S6 where the number of site is normalized by per-site/$\pi(d/2)^2$, where $d = 0.56 \ nm$ is the diameter of the of Pt_nH_x cluster. Whereas, Pt(111) surface is normalized by its surface atomic density (per-site/$a^2 \cos(60°)$ where $a = 0.28 \ nm$).

Table S5 Free energy calculations for the three first most stable $Pt_{13}H_{26}$ clusters. Eelec : electronic energy, ZPE: zero point energy, -TS: vibrational entropic contribution, U: internal energy, F: Helmholtz free energy. The unit in this table is eV. Energies are calculated with the optPBE-vdW functional.

LEME	E_{elec}	ZPE	-TS	U	F
GM0	-124.120	5.360	-1.650	-117.943	-119.593
GM1	-123.946	5.400	-1.746	-117.712	-119.458
GM2	-123.846	5.577	-1.520	-117.508	-119.028

5.10 Methane activation on Pt_{13}

Table S6 Transition states structures and energies activation for methane C-H bond dissociation on bare Pt_{13} clusters. All the transition state structures are located by the Dimer method and verified by vibrational analysis to make sure the structure is a one-order stationary point on the potential energy surface. Then intrinsic reaction coordination (IRC) is also evaluated by displacing the structures along the vibration modes by 0.005 Å and optimizing the structure with small steps dumped MD algorithm. The TS energy here in this table is apparent activation energy, which is defined as $E^{TS} = E(TS) - E(Pt_{13}) - E(CH_4)$. Energies here are calculated with the PBE functional.

Cluster structure	Transition state structure	E^{TS}/eV	E^{TS} at different sites
GM0		0.04	
GM1		0.25	

GM2		0.25	
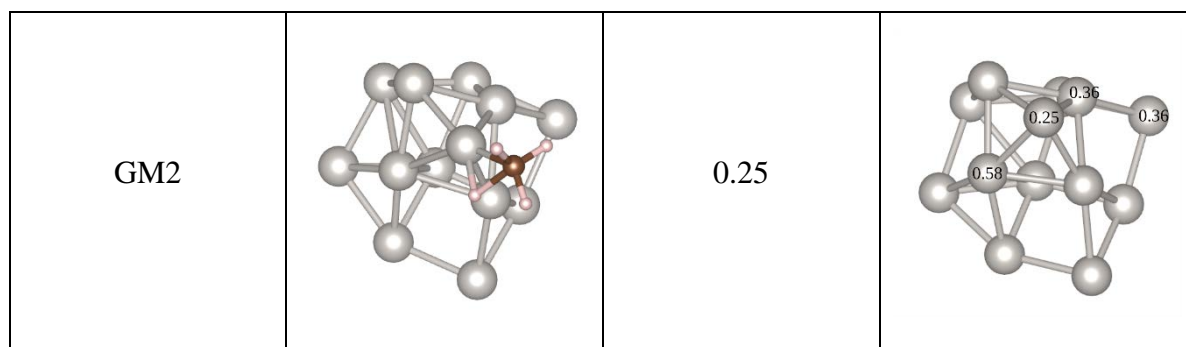
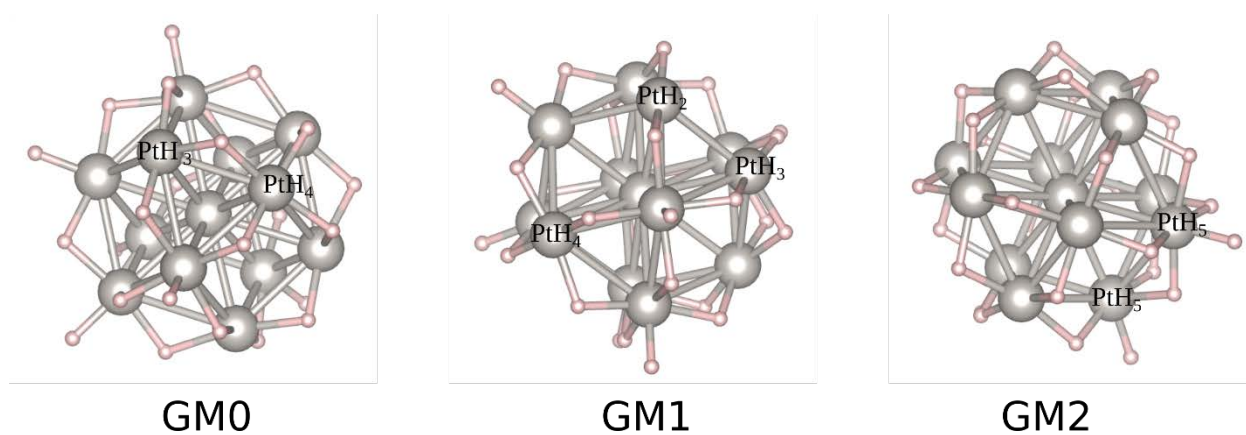## 5.11 Methane activation on $Pt_{13}H_{26}$ clusters.

GM0

GM1

GM2

Figure S17 The different surface sites available for methane activation on $Pt_{13}H_{26}$ clusters. The symbol PtHn means the surface Pt atom is coordinated by n H atoms.

Table S7 Reaction barriers for methane C-H dissociation on $Pt_{13}H_{26}$ clusters, where GM0 indicates the global minimum structure of $Pt_{13}H_{26}$, GM1 indicates the second most stable structures and GM2 indicates the third most stable structure. E_a is the reaction barrier and it is the energy difference between initial configuration (weakly adsorbed CH_4) and the transition state structure. E^{TS} is the apparent activation energy, which is defined as $E^{TS} = E(TS) - E(cluster) - E(CH_4)$. $\Delta E(r)$ is the reaction energy. Two functionals are used, PBE and PBE-dDsC.

Structure and Path	PBE			PBE-dDsC		
	E_a/eV	E^{TS}/eV	$\Delta E(r)$/eV	E_a/eV	E^{TS}/eV	$\Delta E(r)$/eV
GM0 PtH3	1.053	1.018	0.522	1.009	0.891	0.442
GM0 PtH4	1.064	1.019	0.975	1.029	0.892	0.937
GM1 PtH2	0.678	0.629	0.472	0.64	0.516	0.42
GM1 PtH3	0.998	0.958	0.727	0.953	0.842	0.664
GM1 PtH4	1.062	0.991	0.979	0.995	0.835	0.937
GM2 PtH4	1.173	1.138	1.084	1.151	1.011	1.064

S^GM0(PtH3)   S^GM0(PtH4)   S^GM2(PtH4)

S^GM1(PtH2)   S^GM1(PtH3)   S^GM1(PtH4)
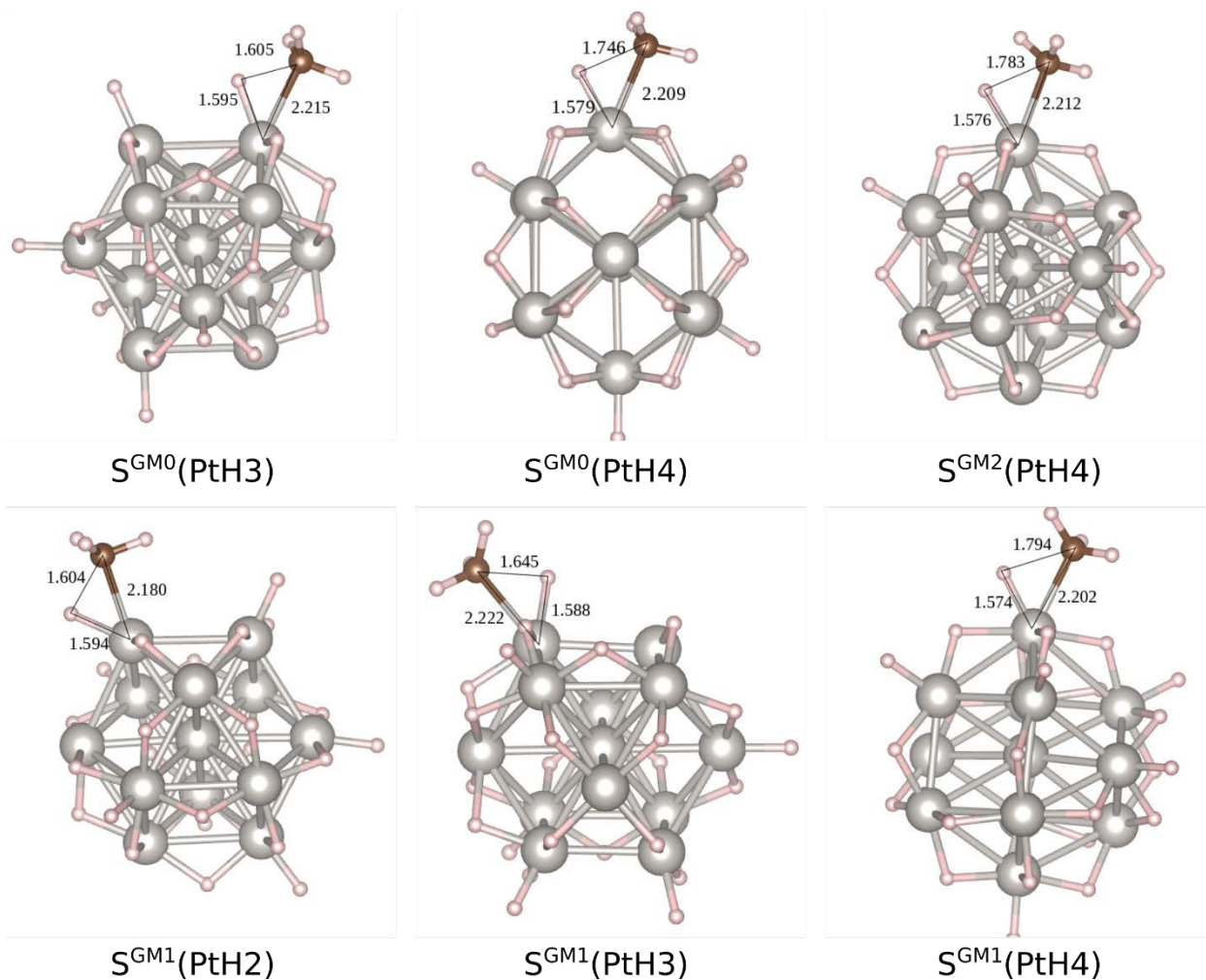
Figure S18 The transition state structures for methane C-H bond dissociation on $Pt_{13}H_{26}$ clusters. The labels of different structures are consistent with Figure 7 in the maintext. The main bond lengths for the transition state structures are also shown with unit Å.
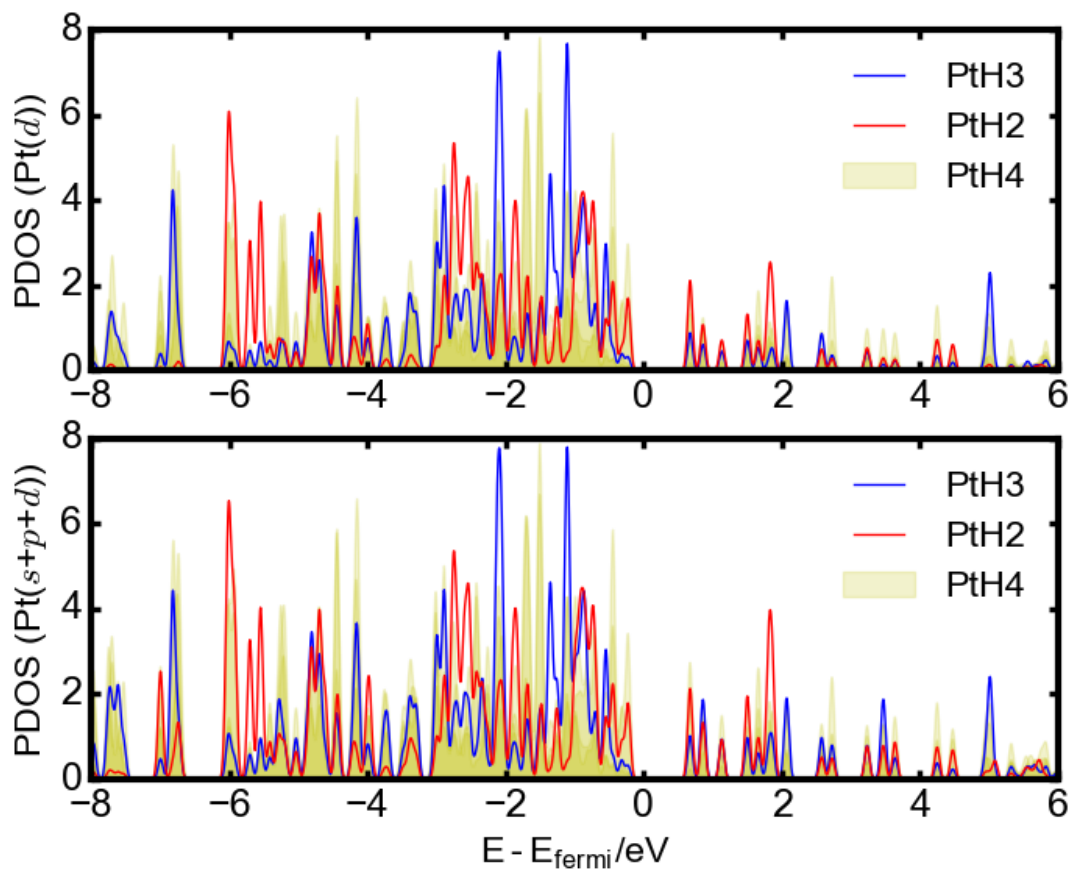
Figure S19: Density of state projectd on the d orbital of te surface Pt atoms (top) and on the surface Pt atom (bottom). Only Pt atoms that are not occupied by a H atom are considered. It shows that d orbitals of PtH2 sites shift towards higher energy compared with that of PtH3. This explains the higher activity of PtH2. PtH4 sites are less active because all the neighboring sites are already occupied by H.

6 References

1.   Kresse, G.; Hafner, J., *Phy. Rev. B* **1994**, *49*, 14251-14269.

2.   Kresse, G.; Furthmüller, J., *Comput. Mater. Sci.* **1996**, *6*, 15-50.

3.   Kresse, G.; Furthmüller, J., *Phys. Rev. B* **1996**, *54*, 11169-11186.

4.   Perdew, J. P.; Burke, K.; Ernzerhof, M., *Phys. Rev. Lett.* **1996**, *77*, 3865-3868.

5.   Klimes, J.; Bowler, D. R.; Michaelides, A., *J Phys Condens Matter* **2010**, *22*, 022201.

6.   Gautier, S.; Steinmann, S. N.; Michel, C.; Fleurat-Lessard, P.; Sautet, P., *Phys. Chem. Chem. Phys.* **2015**, *17*, 28921-30.

7.   Bunău, O.; Bartolomé, J.; Bartolomé, F.; Garcia, L. M., *J. Phys.: Condens. Matter* **2014**, *26*, 196006.

8.   Roduner, E.; Jensen, C., *Magnetochemistry* **2015**, *1*, 28-44.

9.   Piotrowski, M. J.; Piquini, P.; Da Silva, J. L. F., *Phys. Rev. B* **2010**, *81*, 155446.

10.   Steinmann, S. N.; Corminboeuf, C., *J. Chem. Theor. Comput.* **2011**, *7*, 3567-3577.

11.   Hjorth Larsen, A.; Jorgen Mortensen, J.; Blomqvist, J.; Castelli, I. E.; Christensen, R.; Dulak, M.; Friis, J.; Groves, M. N.; Hammer, B.; Hargus, C.; Hermes, E. D.; Jennings, P. C.; Bjerre Jensen, P.; Kermode, J.; Kitchin, J. R.; Leonhard Kolsbjerg, E.; Kubal, J.; Kaasbjerg, K.; Lysgaard, S.; Bergmann Maronsson, J.; Maxson, T.; Olsen, T.; Pastewka, L.; Peterson, A.; Rostgaard, C.; Schiotz, J.; Schutt, O.; Strange, M.; Thygesen, K. S.; Vegge, T.; Vilhelmsen, L.; Walter, M.; Zeng, Z.; Jacobsen, K. W., *J. Phys. Condens. Matter.* **2017**, *29*, 273002.

12.   Behler, J., *Int. J. Quantum. Chem.* **2015**, *115*, 1032-1050.

13.   Artrith, N.; Urban, A., *Comput. Mater. Sci* **2016**, *114*, 135-150.

14.   Hajinazar, S.; Shao, J.; Kolmogorov, A. N., *Phys. Rev. B* **2017**, *95*, 014114.

15.   Deringer, V. L.; Csanyi, G., *Phys. Rev. B* **2017**, *95*, 094203.

16.   Kresse, G.; Hafner, J., *Phy. Rev. B* **1993**, *47*, 558-561.

17.   Vilhelmsen, L. B.; Hammer, B., *J. Chem. Phys.* **2014**, *141*, 044711.

18.   Doye, J. P. K.; Miller, M. A.; Wales, D. J., *J. Chem. Phys.* **1999**, *110*, 6896-6906.

19.   Wales, D. J.; Doye, J. P. K., *J. Phys. Chem. A* **1997**, *101*, 5111-5116.

20.   Goedecker, S., *J Chem Phys* **2004**, *120*, 9911-7.

21.   Nørskov, J. K.; Bligaard, T.; Logadottir, A.; Kitchin, J. R.; Chen, J. G.; Pandelov, S.; Stimming, U., *J. Electrochem. Soc.* **2005**, *152*, J23.